Supporting Information

# Photonic intrinsic chiral flatband with tailorable quality factor and circular dichroism

*Yuexin Sun, Shiwang Yu, Guangzhou Geng, Zhancheng Li*, Yanchun Wang, Wenwei Liu, Hui Liu, Qiang Li, Junjie Li, Hua Cheng*, and Shuqi Chen**

**This file includes:**

**S1. Measured refractive index of amorphous silicon**

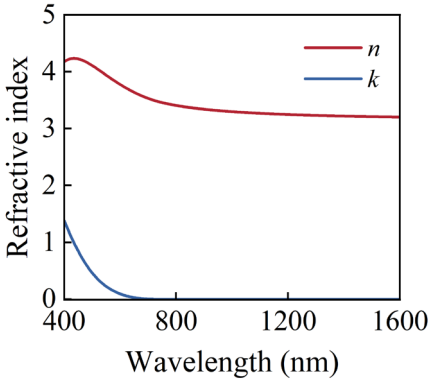


**Figure S1. Measured refractive index of amorphous silicon (*α*-Si).** Real and imaginary refractive index of *α*-Si measured by an ellipsometer.

**S2. Influence of couplings between adjacent resonant modes on the band dispersion of the quasi-guided modes (QGM)**

In our design, two perturbation parameters ($r_2$ and $\alpha_2$) are introduced to induce Brillouin zone (BZ) folding. Both perturbations equivalently break the original hexagonal symmetry, transforming the unit cell into a rectangular lattice. To elucidate how structural variations affect the flatband dispersion, the band structures under different perturbations are calculated, as shown in **Figure S2**. The results demonstrate that, irrespective of the perturbation type or magnitude, structural variations primarily tune the inter-band coupling between the adjacent folded bands and shift the corresponding coupling position. As illustrated in Figures S2a and S2b, a pronounced avoided-crossing behavior emerges between the targeted flatband (red curve) and the adjacent band (blue curve). Increasing $r_2$ shifts the coupling position toward larger $k_x$ values, slightly broadening the flatband region, while varying $\alpha_2$ predominantly modifies the coupling strength, transitioning from strong to weak coupling (Figure S2b). These observations confirm that strong inter-band coupling causes only a minor modulation of the flatband extent along $k_x$; the flatband dispersion remains primarily governed by the standing-wave character of the QGM folded from the guided mode at the boundary of the first Brillouin zone. To quantify the influence of strong coupling, we evaluated the group velocity $v_g = df/dk_x$ of the flatband

mode (Figures S2c and S2d), which demonstrates that the coupling exerts a negligible effect on the flatband dispersion, introducing only a slight change in its overall width. This robustness enables versatile manipulation of the QGM while preserving its flatband characteristics. By comparison, the flatband dispersion of the resonant mode highlighted by the blue curve arises from strong inter-band coupling with the upper adjacent band and exhibits substantial variation with structural perturbations.

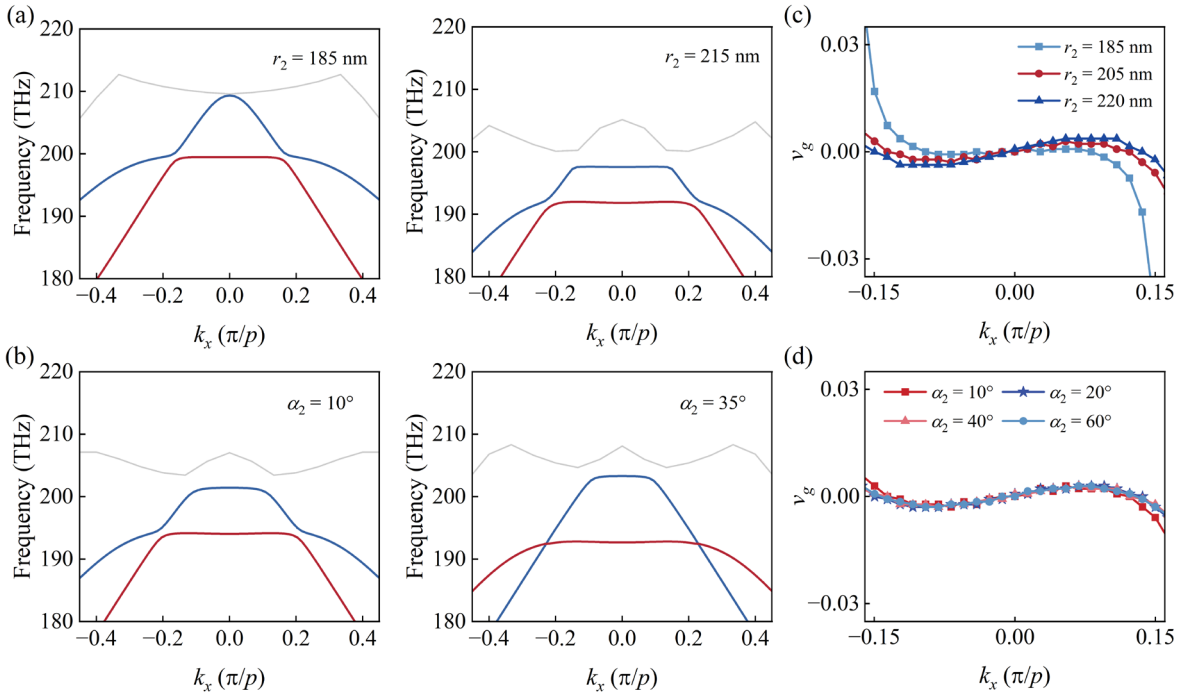


**Figure S2. Band structures of the designed metasurface under different parameter perturbations.** (a) Band structures of the folded lattice for different radius $r_2$ (185 nm and 215 nm), with $r_1$ = 177 nm, $\alpha_1$ = 30°, and $\alpha_2$ = 10°. (b) Band structures of the folded lattice for different rotation angle $\alpha_2$ (10° and 35°), with $\alpha_1$ = 30°, $r_1$ = 177 nm, and $r_2$ = 205 nm. (c, d) Group velocities ($v_g$) of the band highlighted by the red curve in (a) and (b), as functions of (c) $r_2$ and (d) $\alpha_2$.

**S3. Density of states (DOS) analysis of the adjacent resonant modes**

To further verify the high DOS characteristic of the flatband, we calculate the DOS of the two adjacent resonant modes identified by the blue and red lines in the folded band structure in Figure 1f, as shown in **Figure S3**a.[S1] The analysis focuses on the wavevector range

corresponding to the flatband, revealing that the flatband exhibits a DOS approximately three times higher than that of the dispersive band. The DOS along the *x*- and *y*-directions is further compared in Figure S3b, highlighting the more dispersive character of the QGM along the *y*-direction.

The DOS is calculated from the mode spectrum and corresponding Q factors, with each mode represented by a Lorentzian lineshape:

$$L(E, E_i, \Gamma_i) = \frac{1}{\pi} \frac{\Gamma_i}{(E - E_i)^2 + \Gamma_i^2}, \tag{S1}$$

where $E_i$ and $Q_i$ are the eigenenergy and quality factor of the interested mode, and $\Gamma_i = E_i/Q_i$ is the linewidth. The total DOS is then obtained by summing over all sampled wavevectors along the band:

$$g(E) = \sum_i L(E, E_i, \Gamma_i)\Delta k. \tag{S2}$$

Here, $g(E)$ denotes the DOS as a function of energy $E$, where $E$ represents the scanned energy variable used to construct the DOS spectrum. $\Delta k$ denotes the sampling interval in momentum space, and the summation accounts for the contributions from all sampled points in the range of interest.

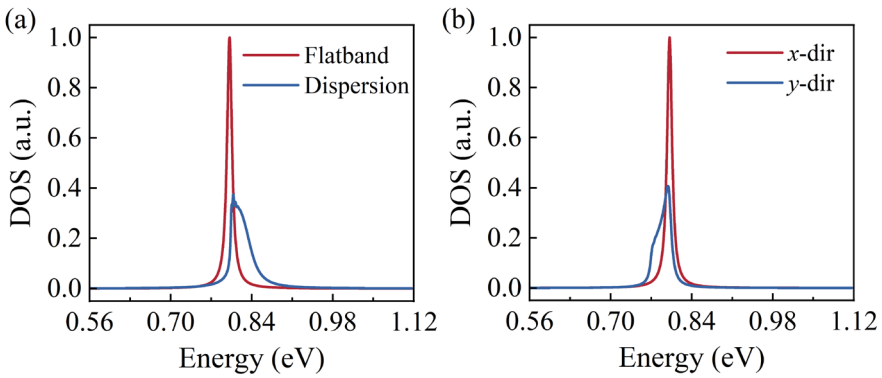


**Figure S3. Comparison of DOS for different cases.** (a) Calculated DOS of the QGM (red line) and the adjacent dispersive mode (blue line), corresponding to the modes highlighted in Figure 1f. (b) DOS of the QGM along the *x* (red) and *y* (blue) directions.

**Section 4. Verification of the intrinsic chirality of the QGM**

To verify the intrinsic chirality of the QGM and its robustness over a wide incident angular range, we calculated the transmission spectra for different polarization components $T_{ij}$ under RCP and LCP incidence across ±14° (**Figure S4**). At the QGM resonance (~1550 nm), the cross-polarized components remain negligible throughout this angular range, and the CD arises from the difference between $T_{RR}$ and $T_{LL}$, confirming the intrinsic chirality of the flatband QGM. We further calculate the transmission spectra under forward (along $-z$ direction) and backward (along $+z$ direction) illumination (Figure S4e, f). In both cases, the CD arises from the difference between $T_{RR}$ and $T_{LL}$, while the cross-polarized components $T_{LR}$ and $T_{RL}$ remain negligible, their relative contributions evolve with changes in the incident direction. The invariance of $\Delta T$ upon reversing the incident direction further confirms the intrinsic character of the QGM.

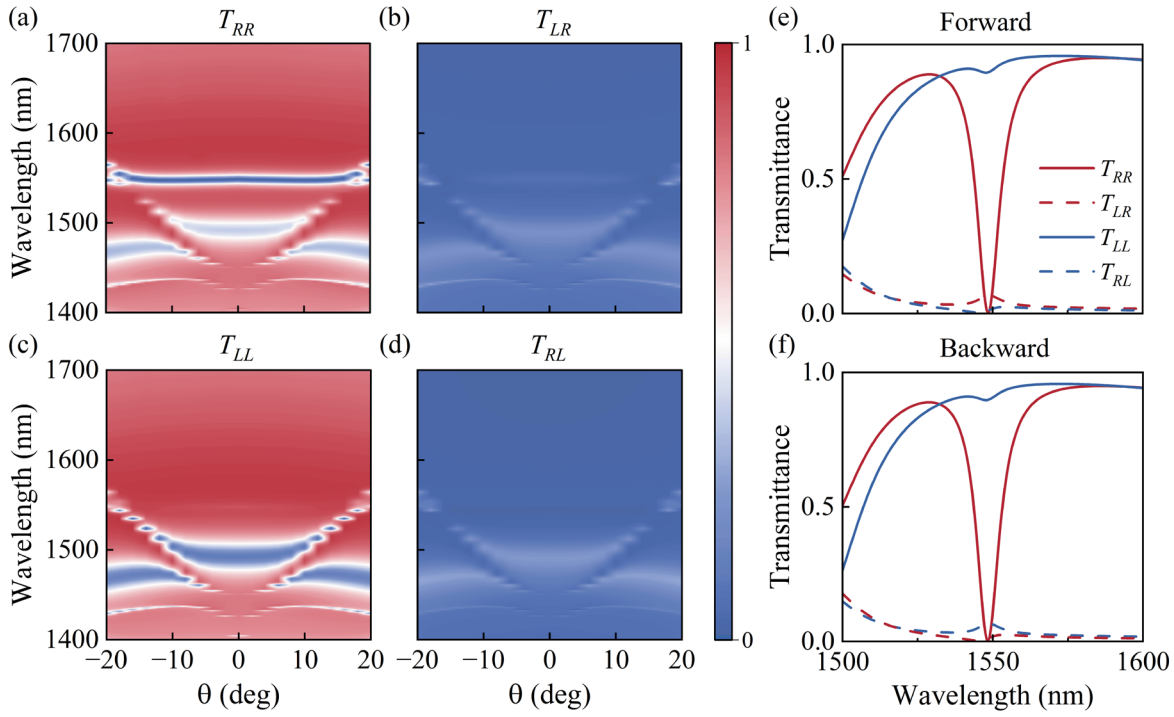


**Figure S4. Verification of intrinsic chirality under different incident angles and illumination directions.** (a-d) The simulated transmission spectra for different polarization components under RCP and LCP incidence: (a) $T_{RR}$, (b) $T_{LR}$, (c) $T_{LL}$, and (d) $T_{RL}$. Here, $T_{ij}$ denotes the square of the amplitude of the transmission coefficient from an incident circularly

polarized (CP) state *j* to a transmitted state *i*. (e, f) The simulated transmission spectra for different polarization components under LCP and RCP normal incidence for (e) forward (–*z* direction) and (f) backward (+*z* direction) illumination.

**S5. Quantitative analysis of the decoupled control of circular dichroism (CD) and the quality (Q) factor of the QGM using temporal coupled mode theory**

To reveal the influence of the structural perturbations on the CD and Q factor of the QGM, we analyze how the structural perturbations $r_2$ and $\alpha_2$ modify the QGM radiation field using temporal coupled-mode theory (TCMT) [S2-S4]. The coupling between the QGM and the incident wave can be expressed as:

$$\frac{da}{dt} = \left(i\omega_0 - \gamma\right)a + \left(\left\langle \kappa \right| * \right)\left| s_+ \right\rangle, \tag{S3a}$$

$$\left| s_- \right\rangle = C\left| s_+ \right\rangle + a\left| d \right\rangle. \tag{S3b}$$

where $\omega_0$ is the resonance frequency, $\gamma$ is the radiative decay rate, $a$ denotes the amplitude inside the resonator, and $C$ is the scattering matrix describing the direct transmission and reflection between the input and output ports. The resonant mode is excited by incoming waves $\left| s_+ \right\rangle$ from two ports with the coupling coefficients $\left| \kappa \right\rangle$ for different polarization states, and radiated to the output ports $\left| s_- \right\rangle$ with the coupling coefficients $\left| d \right\rangle$. The coefficients $\left| d \right\rangle$ and $\left| \kappa \right\rangle$ are not independent. Taking into account time-reversal symmetry and energy conservation conditions, $\left| \kappa \right\rangle = \left| d \right\rangle$ and $\left\langle d \middle| d \right\rangle = 2\gamma$. With incoming waves $\left| s_+ \right\rangle$, the amplitude of the resonant mode can be further expressed as:

$$a = \frac{\left(\left\langle \kappa \right| * \right)\left| s_+ \right\rangle}{i(\omega - \omega_0) + \gamma}. \tag{S4}$$

while the resonant mode decays into the two ports can be obtained as $a\left| d \right\rangle$. Since Q = $\omega_0/2\gamma$, the Q factor of the QGM is correlated to $\left\langle d \middle| d \right\rangle$. Meanwhile, the coupling strengths of the resonant mode to incident waves with different polarization states are decided by the elements

of $|d\rangle$. Therefore, to realize decoupled manipulation of the Q factor of QGM and its coupling strengths to incident waves with different polarization states (for example, left-handed and right-handed circularly polarized waves), it is necessary to independently tune $\langle d|d\rangle$ and the complex amplitudes of the elements of $|d\rangle$.

For the designed metasurface, the light scattered by the two DSS nanostructures are in different elliptically polarized states, denoted as $\mathbf{e}_1$ and $\mathbf{e}_2$, respectively. Thus, the radiation states can be expressed as the coherent superposition of these two contributions:

$$|e_u\rangle = d(r_1,\alpha_1)\mathbf{e}_1(\alpha_1) + d(r_2,\alpha_2)\mathbf{e}_2(\alpha_2), \tag{S5a}$$

$$|e_d\rangle = d'(r_1,\alpha_1)\mathbf{e}_1(\alpha_1) + d'(r_2,\alpha_2)\mathbf{e}_2(\alpha_2). \tag{S5b}$$

where $d(r_1, \alpha_1)$ ($d'(r_1, \alpha_1)$) and $d(r_2, \alpha_2)$ ($d'(r_2, \alpha_2)$) denote the complex coupling coefficients towards the upward (downward) radiation channel, respectively. The existence of the substrate primarily redistributes the total radiated power without modifying its overall variation trend. For simplicity, we restrict our analysis to the upward radiation channel. As shown in Equation S5, we assume that the structural rotation angle $\alpha$ affects only the orientation of the polarization ellipse. Accordingly, the field $\mathbf{e}_2(\alpha_2)$ can be simply expressed as $\mathbf{R}(\alpha_2)\mathbf{e}_2(0)$, where $\mathbf{R}(\alpha_2)$ denotes the rotation matrix. This indicates that the polarization state of $|e_u\rangle$ can be directly tuned through $\alpha_2$. Here, we assume that the complex coupling coefficients $d(r_1, \alpha_1)$ ($d'(r_1, \alpha_1)$) and $d(r_2, \alpha_2)$ ($d'(r_2, \alpha_2)$) remain constant as $\alpha_1$ and $\alpha_2$ varies. Under this assumption, the upward radiation field obtained from the eigen field analysis satisfies:

$$e_{u1} = d(r_1)\mathbf{e}_1(30°) + R(30^\circ)d(r_2)\mathbf{e}_2(0), \tag{S6a}$$

$$e_{u2} = d(r_1)\mathbf{e}_1(30°) + d(r_2)\mathbf{e}_2(0). \tag{S6b}$$

Since $e_{u1}$ and $e_{u2}$ are known from simulations, the components $d(r_1)\mathbf{e}_1(30°)$ and $d(r_2)\mathbf{e}_2(0)$ can be uniquely extracted. These two polarization states therefore serve as basis modes for decomposing and analyzing the radiation behavior of the QGM. To validate our assumption,

we substitute these two basis modes into Eq. (S5a) and calculate the polarization state of $|e_u\rangle$ to make a comparison with the simulated ones, as illustrated in **Figure S5**a. The two exhibit excellent agreement, confirming the validity of describing the upward radiation as a coherent superposition of the two modes.

Moreover, the result further demonstrates that the polarization state of $|e_u\rangle$ can be continuously manipulated from circular to linear polarization by adjusting $\alpha_2$ from 0° to 60° when $r_2$ = 205 nm. Notably, the polarization state becomes purely RCP when $\alpha_2$ equals 5°. Taking into account time-reversal symmetry and energy conservation conditions, the results indicate that for plane-wave excitation along the $-z$ direction, the RCP component is resonantly coupled and strongly reflected, whereas the LCP component is transmitted non-resonantly. In contrast, variation in $r_2$ exerts only a weak influence on the polarization state of the radiation field. Subsequently, we projected the upward radiated field onto the circularly polarized basis, as:

$$|e_u\rangle = d_R\mathbf{e}_R + d_L\mathbf{e}_L, \tag{S7}$$

where $d_R = d(r_1,\alpha_1)d_1^R + d(r_2,\alpha_2)d_2^R e^{-i\alpha_2}$, $d_L = d(r_1,\alpha_1)d_1^L + d(r_2,\alpha_2)d_2^L e^{i\alpha_2}$, in which $d_{1(2)}^R = \mathbf{e}_R^+ \cdot \mathbf{e}_{1(2)}$, $d_{1(2)}^L = \mathbf{e}_L^+ \cdot \mathbf{e}_{1(2)}$. The radiation intensity in the upward direction can be further obtained as $I = |d_R(r_2,\alpha_2)|^2 + |d_L(r_2,\alpha_2)|^2$, as shown in Figures S5b and S5c, which is related to the radiative decay rate $\gamma$ of the QGM as $I \propto 2\gamma$. Furthermore, the results indicate that $I$ remains almost unchanged with the variation of $\alpha_2$, which can be directly manipulated by changing $r_2$. These results indicate that $\langle d|d\rangle$ and the complex amplitudes of the elements of $|d\rangle$ can be modulated by changing $r_2$ and $\alpha_2$, respectively, enabling the decoupled manipulation of Q factor and CD of QGM.

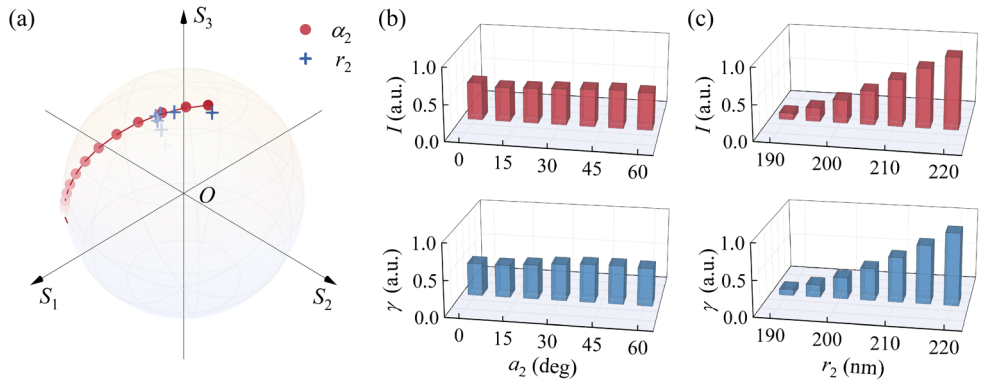


**Figure S5. Modulating the radiation field of the QGM by changing the structural perturbations $r_2$ and $\alpha_2$.** (a) Evolution of the polarization states on the Poincaré sphere as functions of $\alpha_2$ and $r_2$. The red points correspond to the simulated states for $\alpha_2$ swept from 0° to 60° (from dark to light red, in 5° increments), while the blue crosses mark states for $r_2$ swept from 190 to 220 nm (from dark to light blue, in 5 nm steps). The solid red line represents the results calculated based on TCMT. (b, c) Upper panels: Intensities of the upward radiation as functions of (b) $\alpha_2$ and (c) $r_2$. Lower panels: Radiative decay rates of the QGM as functions of (b) $\alpha_2$ and (c) $r_2$.

**S6. Flexible manipulation of the polarization state of the QGM radiation field**

The polarization state of the upward radiation field can be well modulated from right-handed circular to linear polarization by adjusting the structural perturbation $\alpha_2$ from 0° to 60°. By utilizing the mirror image design (named as enantiomer B) of the designed metasurfaces (named as enantiomer A), the polarization state of the upward radiation field can be fully tuned from left-handed to right-handed circular polarization, as illustrated in **Figure S6**. The polarization states within the region ($k_x$ from –0.1 $\pi/p$ to 0.1 $\pi/p$, $k_y$ from –0.1 $\pi/p$ to 0.1 $\pi/p$) are evaluated as a function of $\alpha_2$, as shown in the right panel of Figures S6a and S6b, with the top row representing enantiomer A, and the bottom row enantiomer B. These results reveal two key observations: (i) the polarization states remain invariant across different $k_x$ values within the flatband region, and (ii) they evolve systematically with $\alpha_2$, demonstrating tunable control from circular to linear polarization. Figures S6c and S6d present the calculated Stokes parameters of

enantiomers A and B at the Γ point ($k_x$ = 0 and $k_y$ = 0) as functions of $\alpha_2$, while Figure S6e visualizes the corresponding evolution on the Poincaré sphere, indicating that CD can be fully tunable from ±1 to 0. Such tunability further enables the application of the designed metasurface in nanolasing and thermal emission with tailored and angularly robust polarization states.

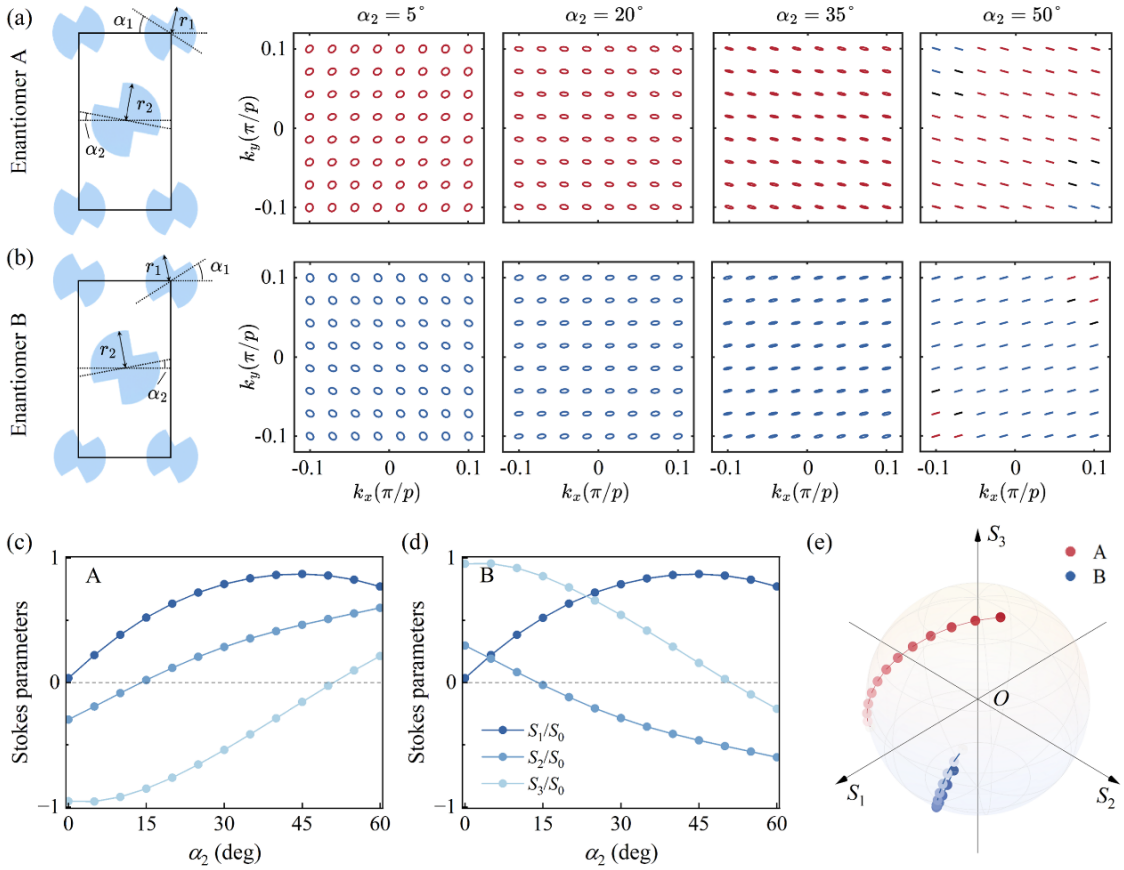


**Figure S6. Evaluation of the polarization state of the QGM under rotation angle perturbation.** (a, b) Left panels: Top views of the DSS structures in a unit cell, showing (a) enantiomer A and (b) enantiomer B with $r_1$ = 177 nm and $r_2$ = 205 nm. Right panels: Corresponding far-field polarization profiles of enantiomers A and B at four representative rotation angles $\alpha_2$ = 5°, 20°, 35°, and 50°. (c, d) Stokes parameters as functions of $\alpha_2$ for (c) enantiomer A and (d) enantiomer B. The gray dashed lines indicate the zero level, and $S_0$ is normalized to 1. (e) Evolution of the polarization states on the Poincaré sphere as $\alpha_2$ varies from 0° (dark color) to 65° (light color) for A and B. Notably, $S_3 \approx -1$ (1) at $\alpha_2$ = 5° for enantiomer A (B), and $S_3 \approx 0$ at $\alpha_2$ = 50°.

**S7. Comparative analysis of the dispersion stability under parameter variations**

To demonstrate the advantage of the chiral QGM in maintaining flatband robustness, we select a representative study on chiral flatbands for comparison.[S5] In that work, two key parameters are introduced to control the dispersion properties: the asymmetry factor and the chirality factor. To enable a direct comparison, we utilize similar parameter definitions. The asymmetry factor $\alpha$ is defined as

$$\frac{1+\alpha}{1-\alpha}=\frac{S_2}{S_1}, \tag{S8}$$

where $S_2$ ($S_1$) denotes the area of the central nanostructure with radius $r_2$ and rotation angle $\alpha_2$ (the surrounding structures with $r_1$ and $\alpha_1$).

The chirality factor $\eta$ is defined as

$$\eta=\frac{\Delta\alpha_1}{\alpha_1}, \tag{S9}$$

where $\Delta\alpha = \alpha_2 - \alpha_1$ represents the angle variation of the central structure while $\alpha_1$ remains unchanged. The specific values of $\alpha$ and $\eta$ are chosen to be the same as those used in Figure S10 of Ref. [S5]. The corresponding calculated angle-resolved CD spectra are shown in **Figure S7**. The results indicate that the flatband dispersion remains well preserved under parameter variations, while only the spectral width and CD magnitude are modulated. Compared with the results reported in Figure S10 of Ref. [S5], the chiral QGMs exhibit improved dispersion stability, which can be attributed to the standing-wave character of the GMs at the Brillouin zone edge, rendering it intrinsically less sensitive to structural perturbations.

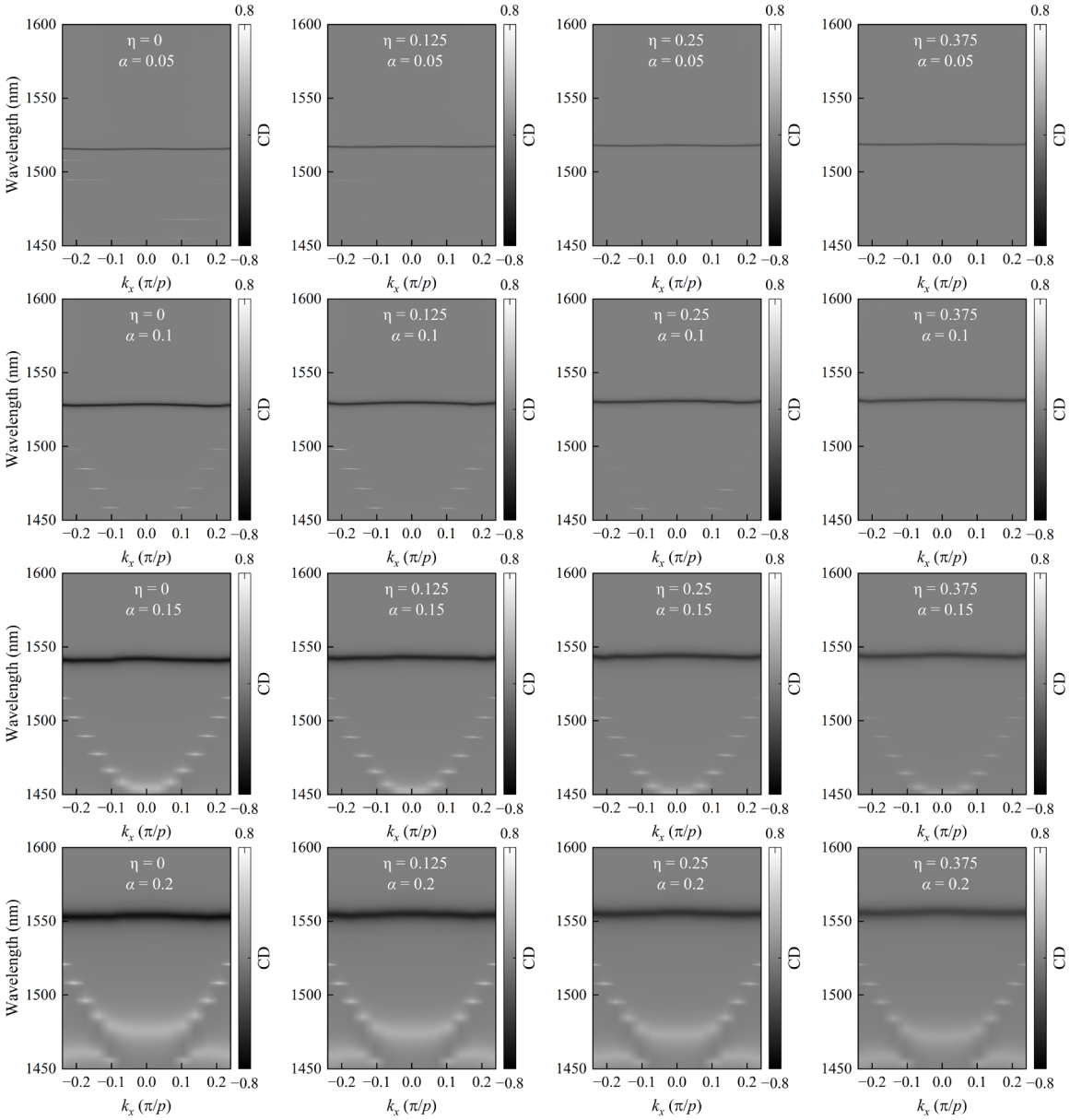


**Figure S7. Calculated angle-resolved CD for different *α* and *η*.** The asymmetry factor $\alpha$ is set to 0.05, 0.1, 0.15, and 0.2, while the chirality factor $\eta$ is set to 0, 0.125, 0.25, and 0.375.

**S8. Analysis of the discrepancies between experimental and simulated results**

The results in Figure 3 indicate modest discrepancies between the experimentally measured and simulated CD and Q factor. In particular, the maximum |CD| measured experimentally is ~0.75, with a Q factor of 95, both averaged over the flatband range of ±14°, whereas the simulation predicts |CD| = 1 and Q = 150. These discrepancies are primarily attributed to fabrication imperfections affecting structural parameters, and to fabrication-induced nonuniformities across the sample area. To validate the concept, we simulated the intrinsic chiral QGMs under

variations of structural parameters, as illustrated in **Figure S8**. The results show that the CD at the resonant wavelength remains robust against structural variations, whereas the Q factor is strongly dependent on the structural width $w$ and inclination angle. Because the inclination angle in the simulations is estimated solely from SEM images, this evaluation is subject to measurement uncertainties, which can account for the differences between the measured and simulated Q factors. It can be seen that when the etching depth $h_1$ deviates from the optimal value of 455 nm, both the Q factor and CD exhibit limited changes. Specifically, within a fabrication tolerance of ±20 nm, the Q factor decreases from 173 to 155 as $h_1$ increases, while CD changes from −0.89 to −1, indicating that the proposed partially etched metasurface is stable against realistic etching depth variations. Notably, the insets of Figures S8a to S8c show that the QGM mode profile remains well preserved during these parameter variations, consistent with the inset in Figure 1f. Furthermore, as shown in Figures S8d to S8f, although the resonant wavelength under normal incidence shifts with these parameter variations, for a fixed set of structural parameters, the resonant wavelength shifts within an incidence angle range of ±14° is limited, indicating that the flatband performance remains effectively constant under these variations.

The manufacturing defects also shift the high-frequency mode, marked as the blue curve in Figure 1f, closer to the QGM in the experimentally measured results. The spectral proximity of these two modes influences the measured transmission spectra and contributes to deviations of the measured CD from the designed values, particularly for the metasurface with |CD| = 1. Furthermore, fabrication-induced nonuniformities and scattering losses contribute to deviations from the simulated response. This broadens the resonance linewidth and modifies the transmission spectra, thereby reducing the measured Q factor and CD. The supercontinuum laser (SC-Pro-M-40, YSL Photonics) was employed as the excitation source in the spectral characterization. For resonances with Q factors in the range of 100–500, the pulse spectral width (~0.07 THz) is much narrower than the resonance linewidth, enabling efficient excitation

of the QGMs with negligible spectral mismatch and minimal impact on experimental tolerance. Overall, the analysis demonstrates that the remaining discrepancies between experiment and simulation are primarily due to fabrication imperfections.

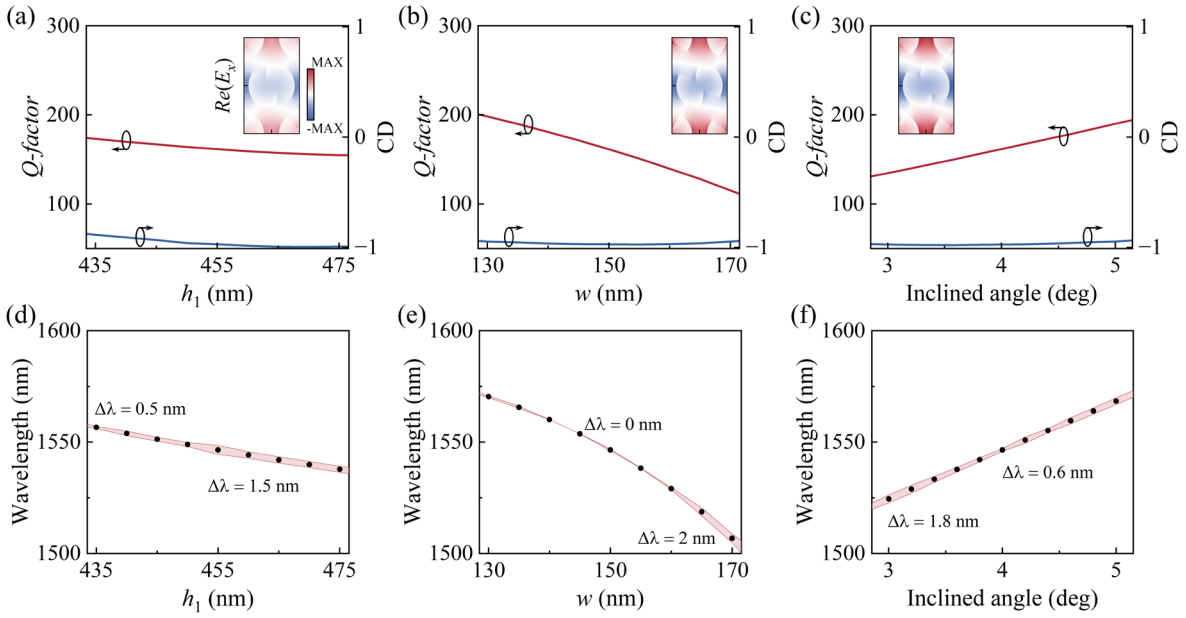


**Figure S8. Influence of structural parameter variations on the resonance characteristics of the flatband QGM.** (a-c) Calculated Q factor and CD as functions of (a) $h_1$, (b) $w$, and (c) inclined angle. The insets show the real part of the $x$-component of the electric field on the middle $x$-$y$ plane of the structures under normal incidence for three cases: $h_1 = 475$ nm, $w = 170$ nm, and inclined angle equal to 5°, respectively. (d-f) Resonant wavelength and the Δλ as functions of (d) $h_1$, (e) $w$, and (f) inclined angle, where $\Delta\lambda = \lambda_{max} - \lambda_0$ denotes the maximum resonance shift within the incidence angle range of ±14° and $\lambda_0$ is the resonant wavelength under normal incidence.

**S9. Experimental demonstration of the CD stability during the Q factor tuning**

We extracted the CD values at different incident angles to show the variation of CD during the Q factor tuning, as shown in **Figure S9**. The CD remains nearly invariant with respect to θ in both simulations and experiments. However, a slight dependence of the CD on $r_2$ is observed experimentally. This minor discrepancy can be attributed to fabrication imperfections affecting structural parameters, and to fabrication-induced nonuniformities across the device area, as we

discussed above.

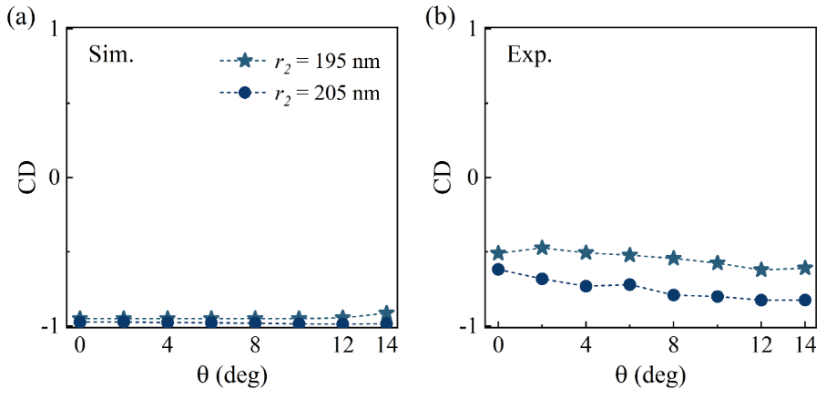


**Figure S9. CD response for different $r_2$.** (a) Simulated CD at the resonant wavelength as a function of incident angle. (b) Measured CD at the resonant wavelength as a function of incident angle.

**S10. Evaluation of THG conversion efficiency**

The THG conversion efficiency is estimated using the Andor spectrometer. First, we verify that the detected photon counts increase linearly with exposure time, as shown in **Figure S10**. This confirms the reliability of the photon-counting measurement and enables quantitative power estimation. To get the detection efficiency of the spectrometer, a reference laser with known output power at the THG wavelength is used. The detected photon counts $N_{ref}$ from the reference laser correspond to a detected power:

$$P_{det,ref} = \frac{N_{ref} hc}{\lambda_{ref} t_{ref}}, \tag{S10}$$

where $h$ is the Planck constant, $c$ is the speed of light, $\lambda_{ref}$ is the wavelength of the reference laser, and $t_{ref}$ is the exposure time. The detection efficiency of the spectrometer is then obtained as:

$$\xi = \frac{P_{det,ref}}{P_{ref}}, \tag{S11}$$

where $P_{ref}$ is the output power of the reference laser.

Based on the calculated detection efficiency, the power of THG can be calculated as

$$P_{\mathrm{THG}} = \frac{N_{\mathrm{THG}} hc}{\lambda_{\mathrm{THG}} t_{\mathrm{THG}} \xi}, \tag{S12}$$

where $N_{\mathrm{THG}}$ is the photon number of the THG signal, and $t_{\mathrm{THG}}$ is the exposure time. Consequently, the THG conversion efficiency, defined as $\eta = P_{\mathrm{THG}}^{average} / P_{pump}^{average}$, is estimated to be 1.1 × $10^{-9}$ for an average pump power of 15.42 mW, while the corresponding normalized conversion efficiency, $\eta_{norm} = P_{\mathrm{THG}}^{peak} / \left(P_{pump}^{peak}\right)^3$, is 1.06 × $10^{-15}$ $W^{-2}$, comparable to previous reports.[S6] These values represent only an approximate estimate, as the transmittance losses of optical elements and the collection efficiency of the objective lens are not included in the calculation. In addition, due to the limited numerical aperture (NA) of the objective, only the zeroth-order diffraction of the THG signal is collected, which may further underestimate the overall conversion efficiency. Notably, rather than pursuing maximum nonlinear signal intensity, this work focuses primarily on the angular robustness of the nonlinear circular CD. To accommodate the relatively broad spectral bandwidth of the excitation femtosecond pulses, moderate Q factors (~100-200) are employed to ensure efficient coupling of the pulse energy into the resonant modes. In principle, significantly higher Q factors could be achieved with a picosecond laser that has a much narrower spectral bandwidth. In general, higher Q resonances provide stronger field enhancement and can therefore further boost the nonlinear response when efficient spectral overlap is maintained.

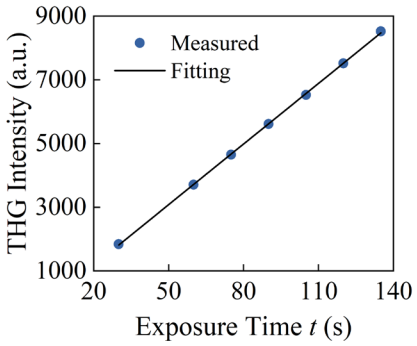


**Figure S10. Measured THG intensity as a function of the exposure time *t*.**

## S11. Summary of the flatband design strategy

| Ref. | Structural Configuration | Supported Modes | Flatband Origin | Spectral Region | Flatband Range | Q factor* | CD* | Decoupled Control |
|---|---|---|---|---|---|---|---|---|
| 39 | Distorted double-disk structures | GMRs QBICs | Mode coupling | MIR (~5.14 μm) | ~±17.5° | ~224 Tunable | × | × |
| 32 | 1D photonic crystal comb structure | super-BICs | Mode coupling | NIR (~1250 nm) | ~±5° | ~500 | × | × |
| 44 | Overlapped double-disk structure | GMRs QBICs | Mode coupling | NIR (~1540 nm) | ~±12° | ~1600 | × | × |
| 46 | Partial etched double S-shaped structures | QBICs | Counter-propagating mode interference | VIS (~720 nm) | ~±5° | ~140 Tunable | ~0.6 Tunable | × |
| 41 | Monoclinic lattice waveguide array | GMRs | The coupled-resonator optical waveguide (CROW) | MIR (~5.30 μm) | ~±12° | ~200 Tunable | ~0.8 Tunable | × |
| This Work | Partial etched double-DSS structures | GMRs | Standing-wave character | NIR (~1550 nm) | ~±14° | ~180 Tunable | ~0.82 Tunable | √ |

**Table S1. Performance comparison of representative flatband designs.** Q factor* denotes the maximum experimentally measured Q factor and its tunability. CD* denotes the maximum experimentally measured CD and its tunability.

## S12. Extension of the chiral flatband QGM design to other spectral regimes

In this design, the intrinsic chiral QGM with flatband dispersion is governed primarily by structural symmetry and periodicity, and can therefore be adapted to different spectral regions. To verify the scalability of our design, we optimized a structure operating in the visible regime, as shown in **Figure S11**. The configuration of the unit cell is identical to that in the main text and is also composed of two DSS nanostructures. The parameters are set as $p$ = 219 nm, $r_1$ = 80 nm, $\alpha_1$ = 20°, $w_1 = w_2$ = 67 nm, $h_1$ = 204 nm, and $h_2$ = 90 nm. The results demonstrate that the intrinsic chiral QGM appears at 710 nm and maintains flatband dispersion within ±15°. Furthermore, the CD and Q factor can be independently controlled, as illustrated in Figures S11c and S11d. These results indicate that the proposed design can be extended to a wide spectral window by appropriately selecting materials and scaling the structural parameters.

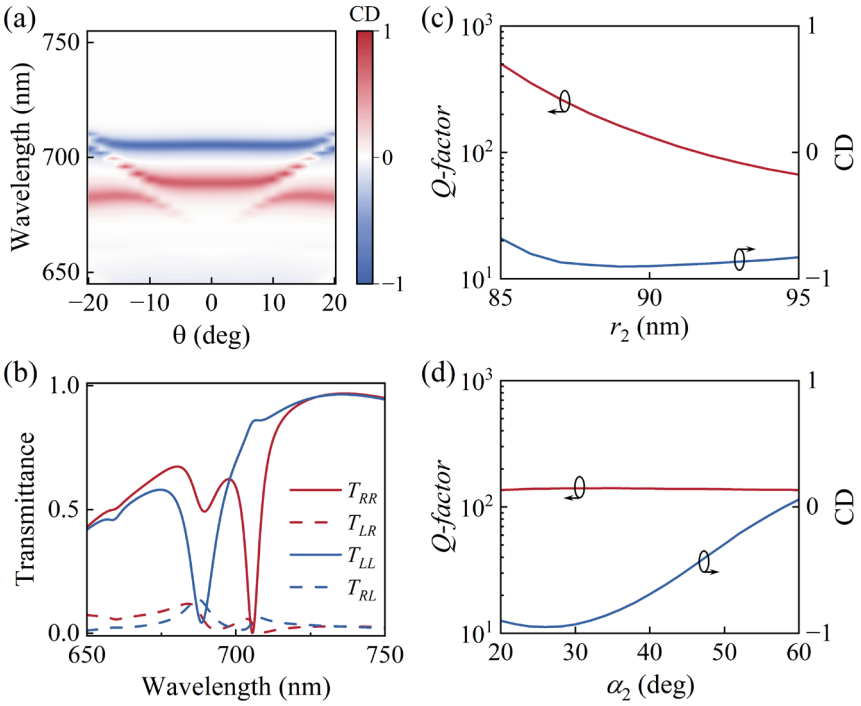


**Figure S11. Characterization of the intrinsic chiral QGM with flatband dispersion in the visible regime.** (a) Simulated angle-resolved CD spectra for $\alpha_2 = 20°$ and $r_2 = 90$ nm. (b) The simulated transmission spectra for different polarization components under normal incidence. (c, d) Calculated CD and Q factor as functions of (c) $r_2$ ($\alpha_2 = 20°$) and (d) $\alpha_2$ ($r_2 = 90$ nm).

**References:**

[S1] T. T. H. Do, Z. Yuan, E. G. Durmusoglu, H. K. Shamkhi, V. Valuckas, C. Zhao, A. I. Kuznetsov, H. V. Demir, C. Dang, H. S. Nguyen, S. T. Ha. Room-Temperature Lasing at Flatband Bound States in the Continuum. *ACS Nano* **2025**, *19*, 19287–19296.
[S2] M. V. Gorkunov, A. A. Antonov, Y. S. Kivshar. Metasurfaces with Maximum Chirality Empowered by Bound States in the Continuum. *Phys. Rev. Lett.* **2020**, *125*, 093903.
[S3] A. Overvig, N. Yu, A. Alu. Chiral Quasi-Bound States in the Continuum. *Phys. Rev. Lett.* **2021**, *126*, 073001.
[S4] S. Fan, W. Suh, J. D. Joannopoulos. Temporal coupled-mode theory for the Fano resonance in optical resonators. *J. Opt. Soc. Am. A* **2003**, *20*, 569–572.
[S5] M. Choi, A. Alù, A. Majumdar. Observation of Photonic Chiral Flatbands. *Phys. Rev. Lett.* **2025**, *134*, 103801.
[S6] B. Zhang, A. Dong, M. Qin, J. Liu, J. Qiu, S. Xiao, W. Huang, H. Li. Wavelength-Locked Quasi-BICs for Enhanced Third-Harmonic Generation in Silicon Metasurfaces. *Adv. Opt. Mater.* **2025**, *14*, e03449.